Journal of the Physical Society of Japan
Vol. 74, No. 4, April, 2005, pp. 1170–1180

Natural Convection in Symmetrically Interconnected Tilted Layers

F. SÁNCHEZ*, C. PÉREZ-ROSALES and A. MEDINA[1†]

Grupo de Medios Porosos y Granulados, Yacimientos Naturalmente Fracturados, Instituto Mexicano del Petroleo, Mexico D.F., 07730, Mexico
[1]*E.T.S. Ingenieros Aeronauticos, Universidad Politecnica de Madrid, Madrid 28040, Spain*

(Received August 3, 2004; accepted January 14, 2005)

The steady thermal convection in symmetrically interconnected, fluid and porous tilted layers has been studied. The layers are surrounded by an impervious rock which is affected by a vertical temperature gradient. Numerical and experimental results were obtained for the temperature distribution in the rock and the convective flow within the layers. Regimes corresponding to small Rayleigh numbers were analyzed because of their relevancy in the geophysical context. The effects of the Rayleigh number and the tilting angle of the layers on the temperature distributions, convection and heat transfer are discussed. Numerical results show a good agreement with the experimental data gotten by the PIV technique and infrared thermography.

KEYWORDS: natural convection, fractured porous media
DOI: 10.1143/JPSJ.74.1170

1. Introduction

There exists a large variety of situations where tilted fluid or porous layers are confined in rocks.[1)] The fluid motions in these systems are of crucial relevancy in the development of important phenomena such as the transport of minerals, radioactive solutes or contaminants. The consequences of this transport, among others, are the cementation and dissolution of minerals in the rock, the change of the features of the layers and the contaminant infiltration into water tables. Moreover, the time scales for transporting passive species, diagenesis and other phenomena in the geological context are strongly modified by the presence of convective flows even when they are weak. A discussion on the diagenetic process and its relation with thermal convection in flat layers has been treated by Wood and Hewett,[2)] who presented the argument that cementation and dissolution in porous sandstones are closely associated with the fluid motion which arises normally in porous bodies. They proposed the free convective motion induced by normal geothermal gradients as the main mass transfer mechanism, which is capable to produce significant changes on porosity and mineral alteration observed in real rocks.[3)]

The study of how some of these processes are modified due to the geothermal gradient was initiated by Davis *et al.*[4)] for the cases of folded periodic-shaped porous layers and by Linz and Woods[5,6)] for the cases of tilted, infinite, flat, porous and fluid layers. The first of these works shows that the geothermal gradient produces significant changes on porosity and mineralogy, and in the second one, an accelerated transport of contaminants was shown to exist. Both works analyzed the effects of the convective motion.

More recently, Luna *et al.*[7)] and Medina *et al.*[8)] have developed the study of thermal convection in tilted, finite layers where the main assumption is that both, the aspect ratio of the layers, $\Gamma = d/h$ (where d is the layer width and h is its length) and the thermal conductivity ratio $\kappa = k_f/k_s$ (where k_s and k_f are the thermal conductivities corresponding to the rock and to the material which fills the layer, respectively), are lower than unity. This is a common situation typically found in water subterranean reservoirs.[9)] This assumption plays a very important role in the theoretical treatment because the heat conduction in the rock and the thermal convection in the layer can be solved separately.

There are many simple geometrical configurations which can be assumed as good approximations for real interconnected fractures and layers. The main aim in the present work is the analysis of the convection in finite tilted layers when they are symmetrically interconnected. This particular condition holds many important characteristics of more complex configurations and their analysis in lab is easy. This study represents a first stage of a research intended for getting a better understanding of the transport phenomena in large networks affected by vertical temperature gradients. Here, two different kinds of folded layers were analyzed: the first one is that of a fluid-filled layer and the last one is a fluid saturated porous layer. In both cases, the convective flow and the inner and outer temperature fields were calculated numerically for the small Rayleigh number regime. Our interest on such a regime obeys to its physical implications on phenomena that take place mainly on geological scales. In spite of the geometrical simplicity, our results show interesting and fundamental features of the convective steady flow and the heat transfer processes that can improve the understanding of several aforementioned geophysical phenomena.

The division of this work is as follows. Next section deals with the statement of the problems of heat conduction in the solid and the fluid flow within the layers. In §3 the dimensionless governing equations are obtained. Section 4 presents the numerical method of solution. In §5 it is described a simple experiment in the fluid layers. Numerical results for the fluid layer and for the saturated porous layer, as well as a comparison between experimental data and numerical results for the fluid layer, are presented in §6. Finally, in §7 the main concluding remarks are given.

2. Statement of the Problem

Consider a two-dimensional horizontal slab of imperme-

*Corresponding author. E-mail: faustoasc@yahoo.com
†On sabbatical leave from IMP.

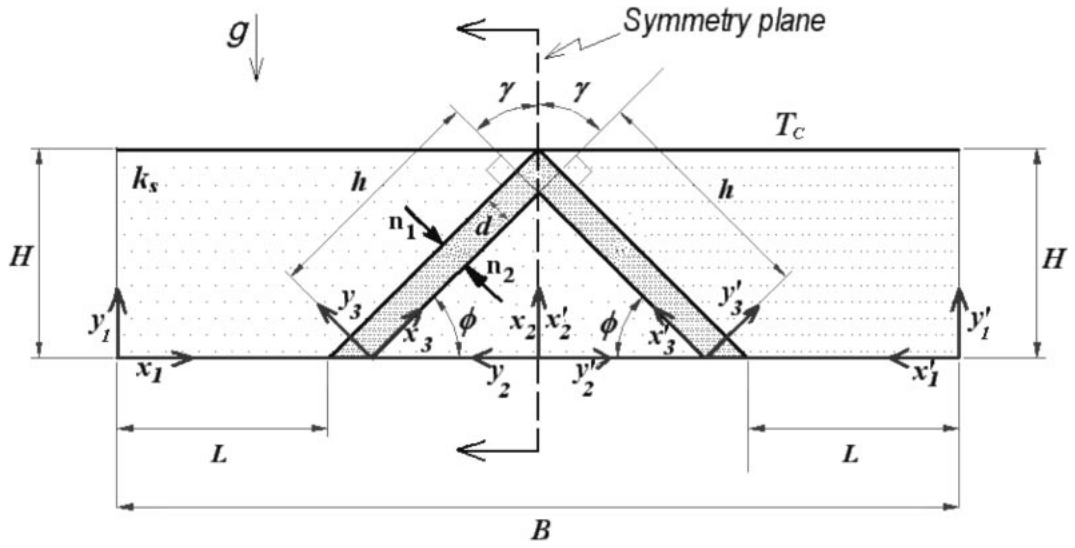

Fig. 1. Schematic of the physical model and coordinate systems.

able rock with finite width B and height H, where $H \ll B$. The rock is crossed by two interconnected layers of width d that run from base to base of the slab at an angle ϕ to the horizontal, as sketched in Fig. 1.

The rock thermal conductivity is k_s and the layer is filled with a material of thermal conductivity k_f. The upper and lower bases of the slab are kept at constant temperatures T_C and $T_H = T_C + \Delta T$, respectively, what would lead to a vertical thermal gradient $G = \Delta T/H$ in the absence of the layer.

Far away from the layers it is expected the isotherms to be horizontal, $\partial T_1/\partial x_1 = 0$ and $\partial T_1/\partial y_1 = G$, but near the layer they must be modified by the effect of the layer itself. For most cases of interest, mainly those related to water and oil reservoirs, the parameters $\Gamma = d/h$ and $\kappa = k_f/k_s$ are small compared with unity but, given the large variety of layers present in a reservoir, the ratio of these two parameters is within a wide range of values, both large and small compared with unity.[1)] In the geophysical context, typical situations are those of a limestone matrix containing either fluid layers of water or oil, or sand layers saturated with any of those fluids. For those conditions $\kappa \sim 0.1$, but combinations for which $\kappa \gg 1$ are also commonly found. It is worth to comment that the limestone typically has a porosity of $\Phi = 0.04$ and a typical porous layer of sand has a porosity about of $\Phi = 0.45$. So, the limestone matrix appears as almost impermeable respect to its inner sand porous layer. Here, the rock matrix is considered as impermeable and cases corresponding to $\kappa/\Gamma \ll 1$ are studied, they physically represent folded bold layers or layers.[10)]

2.1 *Heat conduction in the rock*

As it is shown in Fig. 1, symmetry exists between the right hand side coordinate systems $(1', 2', 3')$ and their corresponding systems at the opposite side $(1, 2, 3)$, for simplicity we just analyzed the last ones, the left hand side. The thermal distribution in the rock obeys the heat diffusion equation, $\nabla^2 T_1 = 0$. For the left external solid region, at the upper edge $T_1 = T_C$, at the lower edge $T_1 = T_H$, the edge at left-hand side (far away from the layer) is adiabatic, $\partial T_1/\partial x_1 = 0$, and on the edge at right hand side (the rock to layer contact surface) the temperature and the heat flux are equal to those experimented by the material in the layer. For the left triangular solid region surrounded by the folded layer, the diffusion equation is solved with the conditions $T_2 = T_H$ at the lower edge, and continuity for the temperature and heat flux at the rock to layer contact surface and at the symmetry plane.

2.2 *Convection in the fluid layer*

Once the problem of the thermal distribution in the rock has been established, we may discuss the convection flow arising in the layers. When a tilted layer is embedded in a solid which is under a vertical thermal gradient, a natural convection flow within the layer must necessarily exist when the thermal conductivity ratio is not equal to 1 ($\kappa \neq 1$) and the layer is neither horizontal ($\phi = 0$) nor vertical ($\phi = \pi/2$), that because for such conditions the isotherms in the fluid at rest are not horizontal. The present work is focused on the analysis of two symmetrically interconnected layers, and for such a case the tilting angle can be neither 0 nor $\pi/2$. Therefore, for the present problem there is no motionless state.

The flow in the fluid layer is modeled by continuity, momentum and energy equations, which respectively are:

$$\nabla \cdot \mathbf{u} = 0, \tag{1}$$

$$(\mathbf{u} \cdot \nabla)\mathbf{u} = -\frac{1}{\rho}\nabla p + \nu \nabla^2 \mathbf{u} + \beta \Delta T \mathbf{g}, \tag{2}$$

$$(\mathbf{u} \cdot \nabla)T = \alpha_f \nabla^2 T. \tag{3}$$

where $\mathbf{u} = (u, v)$ is the two-dimensional velocity, p is the pressure, T is the fluid temperature and $\mathbf{g}$ is the gravity acceleration vector. The fluid has kinematic viscosity ν, density ρ, thermal expansion coefficient β, and thermal diffusivity α_f. We consider constant fluid properties, steady-state flow, and the Boussinesq approximation is applied. This set of equations was solved considering the impermeable and no-slip conditions on all the walls. From experimental experience it was found that there is no mass

exchange between the two layers, at least for the small Rayleigh numbers here studied. So, for the numerical solution an impermeable imaginary wall on the symmetry plane is assumed to exist. For the fluid layer the temperature boundary conditions are $T_3 = T_H$ at the lower wall, zero heat flux at the imaginary wall and continuity for temperature and heat flux at the fluid to solid contact surfaces.

2.3 Convection in the saturated porous layer

The flow in the fluid-saturated porous layer is modeled by continuity, energy and Darcy's equations. Constant fluid properties and steady-state flow are assumed, and the Boussinesq approximation is used. The continuity equation is stated by eq. (1), and the energy equation is given by eq. (3), with α_f substituted by α_m which is equal to the effective thermal diffusivity of the porous medium. The Darcy's equation is:

$$\mathbf{u} = -\frac{K}{\nu}\left(\frac{1}{\rho}\nabla p - \beta \Delta T \mathbf{g}\right) \tag{4}$$

where now $\mathbf{u} = (u, v)$ is the two-dimensional filtration velocity. The fluid which saturates the porous layer has kinematic viscosity ν, density ρ, thermal expansion coefficient β, and the porous layer has a permeability K. All the walls are assumed to be impermeable. It has been considered that because of the symmetry there is not flow at the imaginary wall located on the symmetry plane. The temperature boundary conditions are $T_3 = T_H$ at the lower wall, zero heat flux at the imaginary wall and continuity for temperature and heat flux at the contact surfaces.

3. Dimensionless Equations

A scale analysis shows that the suitable non-dimensional variables are:

For the solid regions:

$$x_1 = \frac{x_1^*}{L}, \quad y_1 = \frac{y_1^*}{H}, \quad \theta_1 = \frac{T_1 - T_C}{T_H - T_C},$$
$$x_2 = \frac{x_2^*}{H}, \quad y_2 = \frac{y_2^*}{H/\tan(\phi)},$$
$$0 < \phi < \pi/2, \quad \theta_2 = \frac{T_2 - T_C}{T_H - T_C}, \tag{5}$$
$$\kappa = \frac{k_f}{k_s}, \quad \Gamma_1 = \frac{H}{L}, \quad \Gamma_2 = \frac{1}{\tan(\phi)}.$$

For the layer region:

$$x = \frac{x_3^*}{h}; \quad y = \frac{y_3^*}{d}; \quad u = \frac{u_3^*}{u_c}; \quad v = \frac{v_3^*}{v_c}; \quad \Gamma = \frac{d}{h}, \tag{6}$$

$$p = \frac{p_3^* d^2}{\rho_0 \alpha^2 \mathrm{Ra}^2}; \quad \theta = \frac{T_3 - T_C}{\Delta T}; \quad \Delta T = T_H - T_C, \tag{7}$$

where u_c and v_c are the characteristic velocities, α is the corresponding thermal diffusivity (α_f or α_m) and Ra is the corresponding Rayleigh number. For the fluid layer $u_c = \alpha_f \mathrm{Ra}\Gamma/d$, $v_c = \Gamma u_c$, and $\mathrm{Ra} = g\beta\Delta T d^3/(\alpha_f \nu)$. For the saturated porous layer $u_c = \alpha_m \mathrm{Ra}/d$, $v_c = \Gamma u_c$, and $\mathrm{Ra} = Kg\beta\Delta T d/(\alpha_m \nu)$.

So, the resulting dimensionless equations for the temperature distributions at the left solid regions are:

$$\Gamma_i^2 \frac{\partial^2 \theta_i}{\partial x_i^2} + \frac{\partial^2 \theta_i}{\partial y_i^2} = 0, \quad i = 1, 2, \tag{8}$$

where 1 and 2 correspond to the external solid region and to the triangular solid region, respectively. Their corresponding boundary conditions couple the thermal problem in the rock with the thermal problem within the cavity. The coupling, however, does not appear at leading order whenever $\kappa/\Gamma \ll 1$. Then the contact surfaces appear as approximately adiabatic and the boundary conditions become $\partial\theta_1/\partial n_1 = 0$ and $\partial\theta_2/\partial n_2 = 0$ at the contact surfaces, where $\partial/\partial n_1$ and $\partial/\partial n_2$ denotes the derivatives normal to the contact surfaces, see Fig. 1. Then, at the contact surfaces the temperature boundary conditions are simplified and the solid regions are solved independently from the fluid region.

If we introduce the stream function, $u = \partial\psi/\partial y$, $v = -\partial\psi/\partial x$, and the Prandtl number, $\mathrm{Pr} = \nu/\alpha_f$, the dimensionless equations for the fluid layer are:

$$\Gamma\left(\frac{\partial\psi}{\partial y}\right)\left[\frac{\partial^3\psi}{\partial x \partial y^2} + \Gamma^2 \frac{\partial^3\psi}{\partial x^3}\right] - \Gamma\left(\frac{\partial\psi}{\partial x}\right)\left[\Gamma^2 \frac{\partial^3\psi}{\partial x^2 \partial y} + \frac{\partial^3\psi}{\partial y^3}\right]$$
$$= \frac{\mathrm{Pr}}{\mathrm{Ra}}\frac{\partial^4\psi}{\partial y^4} + \frac{\mathrm{Pr}\Gamma^4}{\mathrm{Ra}}\frac{\partial^4\psi}{\partial x^4} + \frac{2\mathrm{Pr}\Gamma^2}{\mathrm{Ra}}\frac{\partial^4\psi}{\partial y^2 \partial x^2}$$
$$+ \frac{\mathrm{Pr}\sin(\phi)}{\mathrm{Ra}}\frac{\partial\theta}{\partial y} - \frac{\mathrm{Pr}\Gamma\cos(\phi)}{\mathrm{Ra}}\frac{\partial\theta}{\partial x}, \tag{9}$$

$$\left(\frac{\partial\psi}{\partial y}\right)\frac{\partial\theta}{\partial x} - \left(\frac{\partial\psi}{\partial x}\right)\frac{\partial\theta}{\partial y} = \frac{1}{\Gamma \mathrm{Ra}}\left(\Gamma^2 \frac{\partial^2\theta}{\partial x^2} + \frac{\partial^2\theta}{\partial y^2}\right). \tag{10}$$

On the other hand, after we introduced the stream function, the dimensionless equation for the motion in the saturated porous layer is:

$$\Gamma^2 \frac{\partial^2\psi}{\partial x^2} + \frac{\partial^2\psi}{\partial y^2} = \sin(\phi)\frac{\partial\theta}{\partial y} - \Gamma\cos(\phi)\frac{\partial\theta}{\partial x}, \tag{11}$$

and the dimensionless energy equation is the same one stated by eq. (10).

4. Numerical Method

For solving the fluid-filled layer region problem, eqs. (9) and (10) were linearized assuming that $(\partial\psi/\partial x)$ and $(\partial\psi/\partial y)$ were known from a previous iteration. So, $(\partial\psi/\partial x)$ and $(\partial\psi/\partial y)$ are substituted by $(\partial\psi^0/\partial x)$ and $(\partial\psi^0/\partial y)$, which are renewed after each iteration.

Numerical solutions were obtained by using the conventional centered finite differences method. In order to define a suitable mesh for our non-rectangular geometries, we introduce a simple non-orthogonal set of transformations. For the left external solid region:

$$\xi_1 = \frac{x_1}{1 + \varepsilon_1 \eta_1}, \quad \text{where} \quad \varepsilon_1 = \Gamma_1 \tan\left(\frac{\pi}{2} - \phi\right), \tag{12}$$

$$\eta_1 = y_1, \tag{13}$$

and for the fluid region:

$$\xi = \frac{x}{1 + \varepsilon\eta}, \tag{14}$$

where $\varepsilon = \Gamma\tan(\gamma)$,

$$\eta = y, \tag{15}$$

where γ is the angle formed by the vertical and a line which is perpendicular to the tilted layer, see Fig. 1. So, for the left external solid region, the resulting heat diffusion equation is:

$$\frac{2\varepsilon_1^2\xi_1}{(1+\varepsilon_1\eta_1)^2}\frac{\partial\theta_1}{\partial\xi_1}+\left(\left(\frac{\Gamma_1}{1+\varepsilon_1\eta_1}\right)^2+\left(\frac{\varepsilon_1\xi_1}{1+\varepsilon_1\eta_1}\right)^2\right)\frac{\partial^2\theta_1}{\partial\xi_1^2}-\frac{2\varepsilon_1\xi_1}{1+\varepsilon_1\eta_1}\frac{\partial^2\theta_1}{\partial\xi_1\partial\eta_1}+\frac{\partial^2\theta_1}{\partial\eta_1^2}=0, \tag{16}$$

with the boundary conditions:

$$\text{For } \xi_1=0,\quad 0\le\eta_1\le 1:\ \frac{\partial\theta_1}{\partial\xi_1}=0, \tag{17}$$

$$\text{For } \xi_1=1,\quad 0\le\eta_1\le 1:$$

$$0=\left(\frac{\Gamma_1\cos\left(-\frac{\pi}{2}+\phi\right)}{1+\varepsilon_1\eta_1}-\frac{\varepsilon_1\xi_1\sin\left(-\frac{\pi}{2}+\phi\right)}{1+\varepsilon_1\eta_1}\right)\times\frac{\partial\theta_1}{\partial\xi_1}+\sin\left(-\frac{\pi}{2}+\phi\right)\frac{\partial\theta_1}{\partial\eta_1}, \tag{18}$$

$$\text{For } \eta_1=0,\quad 0\le\xi_1\le 1:\theta_1=1, \tag{19}$$

$$\text{For } \eta_1=1,\quad 0\le\xi_1\le 1:\theta_1=0. \tag{20}$$

For the fluid layer, the equation for motion at the non-orthogonal frame is:

$$A\frac{\partial^4\psi}{\partial\xi^4}+B\frac{\partial^4\psi}{\partial\xi^3\partial\eta}+C\frac{\partial^3\psi}{\partial\xi^3}+D\frac{\partial^2\psi}{\partial\xi^2}+E\frac{\partial^3\psi}{\partial\xi^2\partial\eta}+F\frac{\partial^4\psi}{\partial\xi^2\partial\eta^2}+G\frac{\partial\psi}{\partial\xi}+H\frac{\partial^2\psi}{\partial\xi\partial\eta}+I\frac{\partial^3\psi}{\partial\xi\partial\eta^2}+J\frac{\partial^4\psi}{\partial\xi\partial\eta^3}+K\frac{\partial^3\psi}{\partial\eta^3}+L\frac{\partial^4\psi}{\partial\eta^4}=M\frac{\partial\theta}{\partial\xi}+N\frac{\partial\theta}{\partial\eta}, \tag{21}$$

where functions A to N are given in the Appendix. The energy equation is:

$$R\frac{\partial\theta}{\partial\xi}+S\frac{\partial^2\theta}{\partial\xi^2}+T\frac{\partial^2\theta}{\partial\xi\partial\eta}+U\frac{\partial^2\theta}{\partial\eta^2}+V\frac{\partial\theta}{\partial\eta}=0. \tag{22}$$

Functions R to V are given in the Appendix. The boundary conditions at the non-orthogonal frame are:

$$\frac{\partial\psi}{\partial\eta}=0\quad\text{and}\quad\frac{\partial\psi}{\partial\xi}=0\quad\text{with}\quad\psi=0\quad\text{for}\quad\left\{\begin{array}{ll}\xi=0, & 0\le\eta\le 1\\ \xi=1, & 0\le\eta\le 1\\ \eta=0, & 0<\xi<1\\ \eta=1, & 0<\xi<1\end{array}\right\}, \tag{23}$$

$$\text{For } \xi=0,\quad 0\le\eta\le 1:\theta=1, \tag{24}$$

$$\text{For } \xi=1,\quad 0\le\eta\le 1:$$

$$0=\left(\frac{\Gamma\cos(-\gamma)}{1+\varepsilon\eta}-\frac{\varepsilon\xi\sin(-\gamma)}{1+\varepsilon\eta}\right)\frac{\partial\theta}{\partial\xi}+\sin(-\gamma)\frac{\partial\theta}{\partial\eta}, \tag{25}$$

$$\text{For } \eta=0,\quad 0<\xi<1:\theta=1, \tag{26}$$

$$\text{For } \eta=1,\quad 0<\xi<1:\theta=\theta_1(\xi)|_{\xi_1=1}. \tag{27}$$

On the other hand, for the saturated porous layer the equation for motion at the non-orthogonal frame is:

$$A\frac{\partial\psi}{\partial\xi}+B\frac{\partial^2\psi}{\partial\xi^2}+C\frac{\partial^2\psi}{\partial\xi\partial\eta}+D\frac{\partial^2\psi}{\partial\eta^2}=E\frac{\partial\theta}{\partial\xi}+F\frac{\partial\theta}{\partial\eta}, \tag{28}$$

where functions A to F are given in the Appendix. The energy equation is the same stated by eq. (22), functions R to V for this case are also given in the Appendix. The boundary conditions for the saturated porous layer are:

$$\frac{\partial\psi}{\partial\eta}=0\quad\text{for}\quad\left\{\begin{array}{ll}\xi=0, & 0\le\eta\le 1\\ \xi=1, & 0\le\eta\le 1\end{array}\right\}, \tag{29}$$

$$\frac{\partial\psi}{\partial\xi}=0\quad\text{for}\quad\left\{\begin{array}{ll}\eta=0, & 0<\xi<1\\ \eta=1, & 0<\xi<1\end{array}\right\}, \tag{30}$$

$$\text{For } \xi=0,\quad 0\le\eta\le 1:\theta=1, \tag{31}$$

$$\text{For } \xi=1, 0\le\eta\le 1:$$

$$0=\left(\frac{\Gamma\cos(-\gamma)}{1+\varepsilon\eta}-\frac{\varepsilon\xi\sin(-\gamma)}{1+\varepsilon\eta}\right)\frac{\partial\theta}{\partial\xi}+\sin(-\gamma)\frac{\partial\theta}{\partial\eta}, \tag{32}$$

$$\text{For } \eta=0,\quad 0\le\xi\le 1:\theta=1, \tag{33}$$

$$\text{For } \eta=1,\quad 0\le\xi\le 1:\theta=\theta_1(\xi)|_{\xi_1=1}. \tag{34}$$

For the new coordinates ξ–η, our non-rectangular geometries are transformed into squares, so, $0\le\xi\le 1$, and $0\le\eta\le 1$, what allowed us to use a simple mesh in the numerical code. It was used a mesh of 125×30 nodes, and the residual lower than 10^{-6} for each equation was the convergence criteria.

5. Fluid Layer Experimental Setup

The experimental setup that meets with the assumed conditions in the theoretical model consists of a copper plate (thermal conductivity $k_f=401\,\mathrm{W\,m^{-1}\,K^{-1}}$) vertically placed with length of $B=0.76\,\mathrm{m}$, height of $H=0.164\,\mathrm{m}$ and thickness of 0.04 m. The plate was provided with an internal folded gap of width $d=0.005\,\mathrm{m}$ and length $h=0.2\,\mathrm{m}$, with $\phi=45^\circ$, so the aspect ratio is $\Gamma=0.025$. In order to get two-dimensional flow the thickness of the plate was sufficiently large respect to d. The slit was sealed by very thin transparent plastic sheets glued to the front and rear faces of the copper plate. As this plastic is transparent it was possible to visualize the flow within the gap. Horizontals channels were carved at the upper and lower edges of the copper plate where thin cooper pipes were tightly placed. Our plate, shown in Fig. 2, was provided with four copper pipes, a couple of them at the upper edge and the rest at the lower one. Constant temperatures were imposed at the edges by recirculating through the pipes water from thermal baths. Each couple of pipes worked in counter flow, the upper pipes cooled the plate and the lower ones heated it.

The fluid within the gap was glycerine, which for $T=305\,\mathrm{K}$ has the following properties: density $\rho=1257\,\mathrm{kg\,m^{-3}}$, thermal conductivity $k_f=0.286\,\mathrm{W\,m^{-1}\,K^{-1}}$, thermal expansion coefficient $\beta=0.485\times10^{-3}\,\mathrm{K^{-1}}$, thermal diffusivity $\alpha=9.2\times10^{-8}\,\mathrm{m^2\,s^{-1}}$, kinematic viscosity $\nu=457\times10^{-6}\,\mathrm{m^2\,s^{-1}}$ and Prandtl number $\mathrm{Pr}=4943$. Under these conditions, the thermal conductivity ratio is $\kappa=7.1\times10^{-4}$, so $\kappa/\Gamma=0.0285\ll 1$.

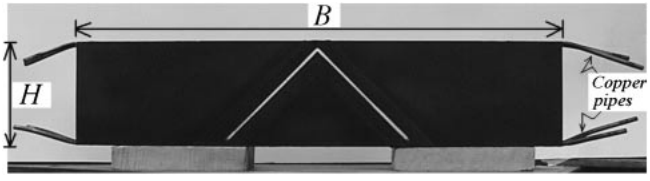

Fig. 2. Experimental model.

For measuring the overall temperature distribution on the plate an infrared camera model FLIR ThermaCam™ PM595 was used. The velocity in the gap was estimated by Particle Image Velocimetry (PIV). The glycerine was seeded with null buoyancy conifer pollen 50 μm mean particle size. These particles were visible as little white spots when a continuous light from an halogen lamp illuminated the gap. The fluid motion at different locations throughout the gap was recorded by a 30 expositions per second digital video camera.

The copper plate was thermally insulated with polyurethane foam plates 0.04 m thick. The thermal baths were turned on and kept working as long as 6 h before the window on a polyurethane foam plate were removed and measurements were done. Then several infrared images and the particle motion were recorded. Successive pairs of images from the movie were used to get the velocity field via cross-correlation. The ThermaCam™ software was used to analyze the infrared images and temperature profiles at different locations on the plate were estimated.

6. Results

6.1 Temperature distribution in the rock

A sample numerical solution for $\phi = \pi/4$ is shown in Fig. 3(a). This numerical result for the temperature distribution in the solid regions was confirmed by experiments. An infrared image of the experimental device is shown in Fig. 3(b). Clearly qualitative agreement with Fig. 3(a) is quite good. Numerical results and thermographies show the important change of the isotherms in the rock near the layer.

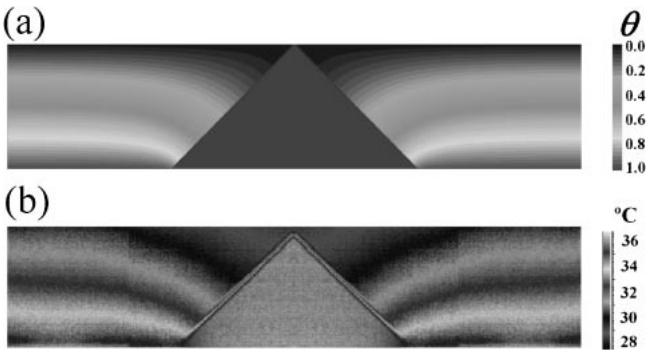

Fig. 3. Temperature distribution in the rock. (a) Numerical result corresponding to $\kappa \ll 1$, $\phi = \pi/4$. (b) Experimental temperature distribution in the rock near the gaps (layers). $\Delta T = 6.5$ K, $\phi = \pi/4$.

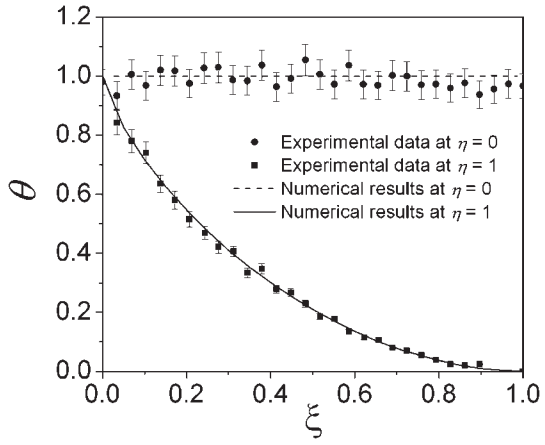

Fig. 4. Numerical and experimental dimensionless temperature profiles at the longitudinal contact surfaces corresponding to the left hand side when $\phi = \pi/4$. Experimental temperature profiles were measured for $\Delta T = 6.5$ K, and the error bars correspond to ±5%.

Far away from the layer the vertical temperature gradient is nearly constant (nearly horizontal isotherms), and as the layer is closer the isotherms are strongly affected. Moreover, the existence of a single isotherm in the triangular solid region is evident.

Quantitative agreement is shown in Fig. 4, where numerical and experimental dimensionless temperature profiles at the solid–fluid contact surfaces are presented. There, a direct comparison between the experimental data (symbols) and numerical results (curves) is shown. These measured thermal profiles are those experimented by the material in the layer. It is worth to observe the temperature differences between opposite points on the contact surfaces. Indeed, these are of the order of ΔT and vary with ξ, and the critical change (equal to ΔT) takes place at the upper corner ($\xi = 1$), Fig. 4.

The tilting angle ϕ plays an important role on the thermal distribution in the rock as it is shown in Fig. 5. Far away from the layers the vertical temperature gradient is constant (horizontal isotherms), and as the layers are closer the isotherms are affected, strongly for small values of ϕ and weakly for large ones.

The heat flux across the layer due to this temperature difference, which has been neglected in the theoretical analysis, is of order $k_f \Delta T/d$. This flux is small compared to the characteristic heat flux through the solid, $q_s = k_s \Delta T/H$, when $\kappa \ll \Gamma$, as it was advanced before. If this condition is

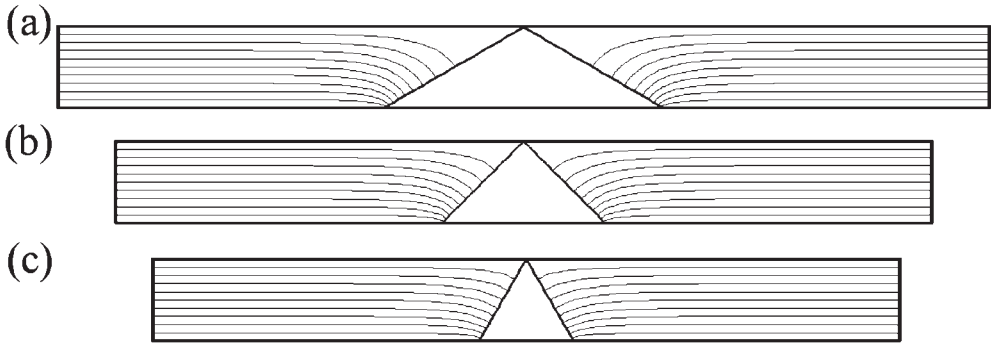

Fig. 5. Effect of the angle ϕ on the temperature distribution in the rock near the gap (layer). (a) $\phi = \pi/6$. (b) $\phi = \pi/4$. (c) $\phi = \pi/3$. The upper edge is at $\theta = 0$, the lower one is at $\theta = 1$ and the isotherms are 0.1 equally spaced.

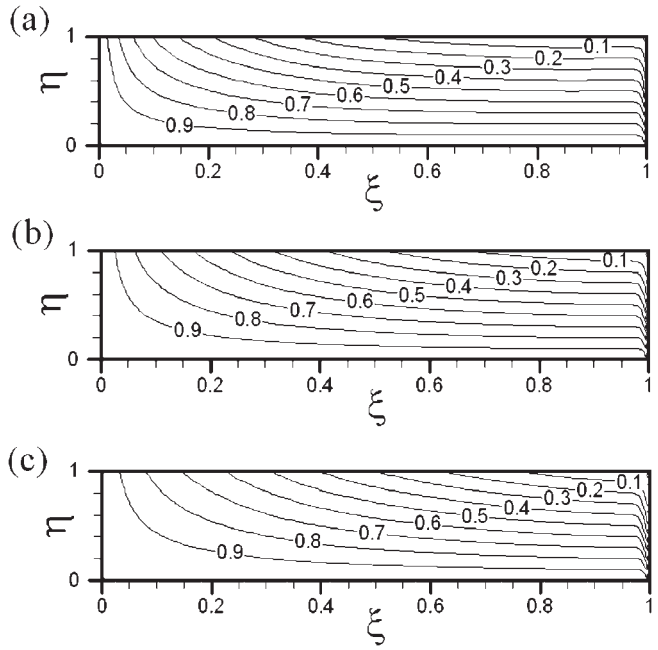

Fig. 6. Dimensionless temperature distribution within the fluid layer in the non-orthogonal coordinate system. Effect of the tilting angle ϕ when $\kappa \ll 1$, $\Gamma = 0.01$. (a) $\phi = \pi/6$. (b) $\phi = \pi/4$. (c) $\phi = \pi/3$. These plots also correspond to the cases of saturated porous layers.

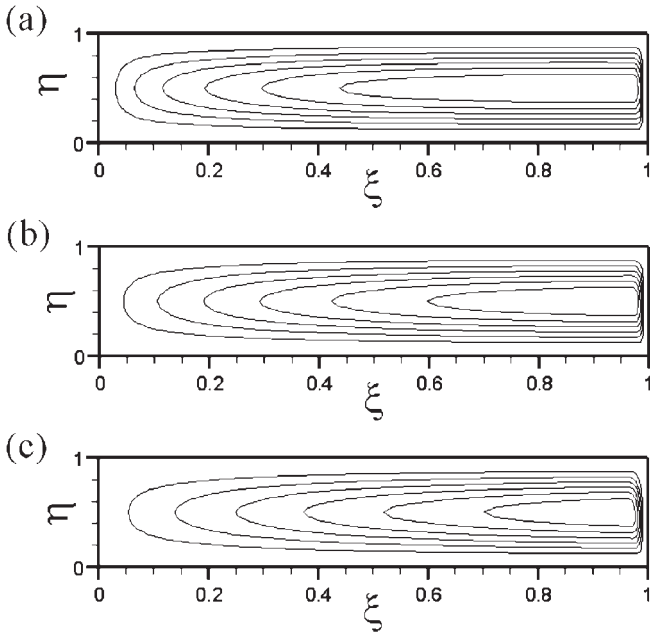

Fig. 7. Effect of the angle ϕ on the convective flow within the fluid layer. For all cases $\mathrm{Pr} = 0.3645$, $\kappa \ll 1$, $\Gamma = 0.01$. (a) $\phi = \pi/6$. (b) $\phi = \pi/4$. (c) $\phi = \pi/3$. These plots are valid for $10^{-1} \leq \mathrm{Ra} \leq 10$.

not satisfied, then the heat transfer problems in the solid and in the layer are coupled and should be solved simultaneously.

6.2 *The fluid layer*

As the tilting angle ϕ affects the temperature distribution in the rock, this angle itself has an important effect on the temperature distribution within the fluid layer, Fig. 6. It was found that diffusion is the main mean for the heat transfer in the layer, as it was expected. Indeed, since the Rayleigh numbers here analyzed are small, $10^{-1} \leq \mathrm{Ra} \leq 10$, the resulting weak convective flows do not affect the isotherms at all. So, plots in Fig. 6 were found to be valid for that range of the Rayleigh number. As it was noticed before, for the present problem there is no motionless state, however, such a state seems to be a good reference case to compare to the convective condition. The motionless state represents the case for which the fluid layer is replaced by a solid layer with the same thermal conductivity. Then, it was found that the temperature distributions shown in Fig. 6 match the solutions calculated for conditions where the motionless state exists in the layer (pure conduction heat transfer), what confirms that the convection flow is under the conduction regime.

The resulting fluid motion is clearly two-dimensional as it can be seen in Fig. 7, where numerical results for the stream function, in the non-orthogonal coordinate system, are shown for different values of ϕ, when $\mathrm{Pr} = 0.3645$, $\kappa \ll 1$, $\Gamma = 0.01$. As the layer is under the conduction regime, plots in Fig. 7 are valid for $10^{-1} \leq \mathrm{Ra} \leq 10$. So, because of this condition, the Rayleigh number do not affect the shape of the convective patterns but the angle ϕ does. Actually, Fig. 7 corresponds to conditions commonly found in geothermal systems.[1,4] The Prandtl number used for the numerical solution, $\mathrm{Pr} = 0.3645$, corresponds to a typical value for oil at deposit conditions, what makes this result particularly interesting because of its possible practical applications.

As it could be expected from the temperature distributions in the rock, the circulation patterns are counterclockwise, the flows arise longitudinally near the lower wall (where $\theta = 1$) throughout the layer and descend near the upper wall where the temperature is lower. Close to the upper corner the flow suddenly changes its direction while at the lower region the change in direction is very slow and soft. Details of the numerical streamlines near the upper corner are presented in Fig. 8(a). Here the coordinate system is the original one, what allows us to appreciate the flow within the real layer geometry. The experimental velocity field and streamlines for this same region are compared in Fig. 8(b). Both, experimental and numerical results correspond to the same conditions. The experimental measurement, Fig. 8(b), shows

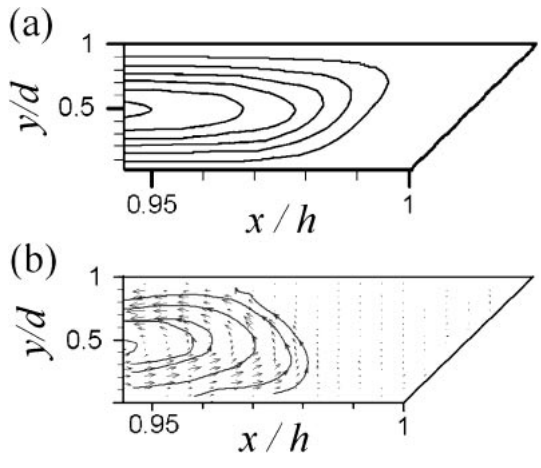

Fig. 8. Near the upper corner. (a) Numerical streamlines. (b) Experimental velocity field and streamlines. $\mathrm{Ra} = 84$, $\mathrm{Pr} = 4950$, $\Gamma = 0.025$.

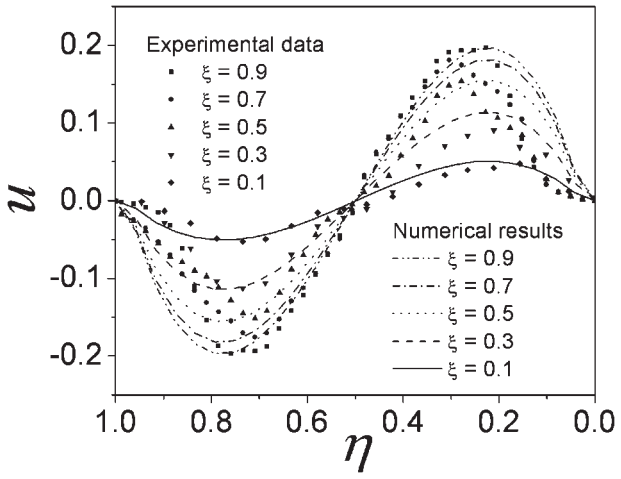

Fig. 9. Longitudinal velocity profiles at different locations within the fluid layer when Ra = 84, Pr = 4950, $\Gamma = 0.025$. Numerical and experimental results.

that practically there is a stagnant region at the upper corner and no mass exchange between the two layers was found, a useful condition already applied for the numerical solution.

A comparison between numerical results and experimental data for the longitudinal dimensionless velocity profiles within the layer are presented in Fig. 9. A good agreement between them is plain for $0.2 \leq \eta \leq 0.8$, out of this range there is an important discrepancy. For getting a completely trusty measurement from the PIV technique is necessary to use a laser sheet as the lighting source, and because of the design of our simple experimental setup we had to use just a continuous (spread) light from an halogen lamp for illuminating the gap. So the inherent parallax from the camera point of view and such an illumination caused an erroneous measurement particularly evident near the walls where the parallax is maximum. Despite this inconvenient, this comparison allows to trust on the numerical solutions. The velocity profiles are symmetrical respect to the middle plane $\eta = 0.5$, and as the fluid is warmed while it travels along the lower wall, the flow is faster at the upper region. The experimental transversal velocity is not shown because it is so small, what makes difficult to measure it, that because of the noise.

Due to the fact that the layer is under the conduction regime, it was found that the dimensionless velocity does not change with the Rayleigh number. Therefore, the velocity profiles presented in Fig. 10 are valid for $10^{-1} \leq \mathrm{Ra} \leq 10$, when Pr = 0.3645, $\Gamma = 0.01$ and $\phi = \pi/4$. The effect of the Rayleigh number on the *actual* velocity is considered in the definition of the dimensionless velocity itself. Figure 10(a) shows the longitudinal dimensionless velocity profiles within the layer. The transversal velocity profile at the middle plane, $\eta = 0.5$ is shown in Fig. 10(b). This profile allows to observe how fast the flow changes its direction at the upper corner and how slow this motion at the lower one is. The tilting angle ϕ affects the longitudinal dimensionless velocity as it is shown in Fig. 11, where all profiles correspond to the velocity u at the middle plane, $\xi = 0.5$. Again, these plots are valid for $10^{-1} \leq \mathrm{Ra} \leq 10$ with Pr = 0.3645, $\Gamma = 0.01$. If the angle ϕ increases the temperature

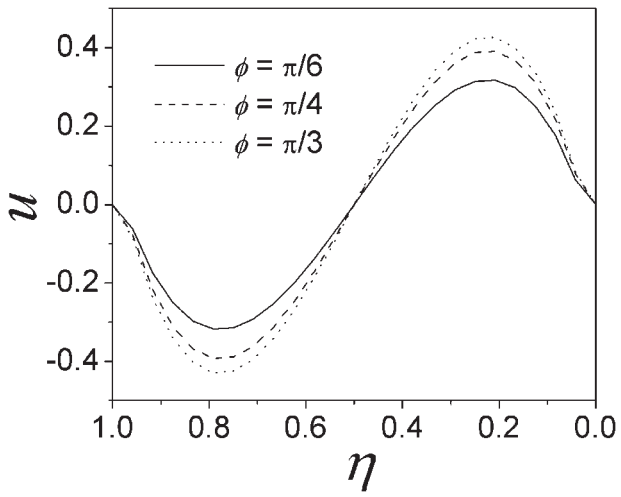

Fig. 11. Effect of the angle ϕ on the longitudinal velocity within the fluid layer. For all cases Pr = 0.3645, $\Gamma = 0.01$. All profiles correspond to the velocity u at the middle plane, $\xi = 0.5$. These plots are valid for $10^{-1} \leq \mathrm{Ra} \leq 10$.

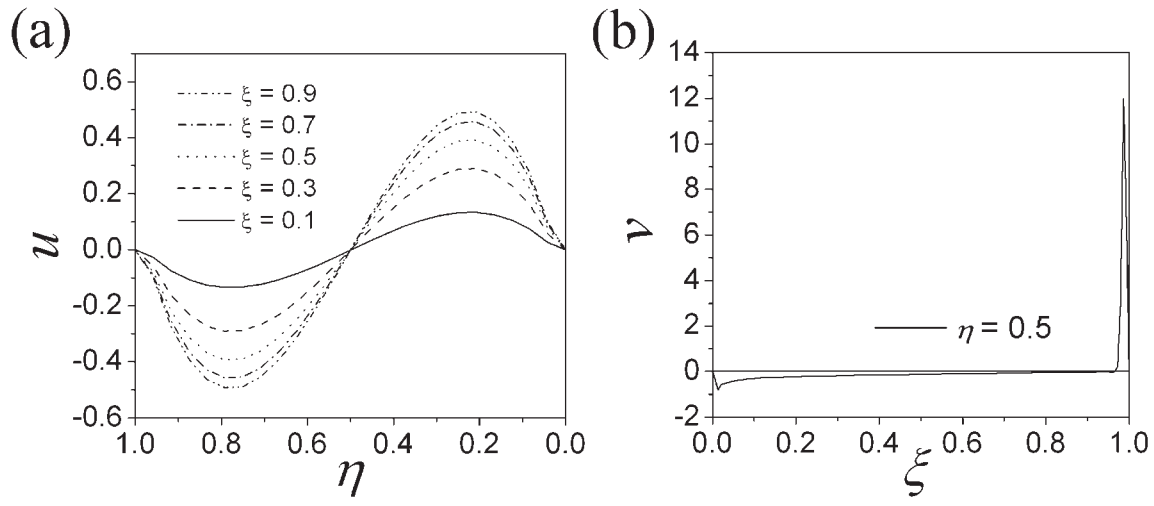

Fig. 10. Velocity profiles at different locations within the fluid layer when Pr = 0.3645, $\Gamma = 0.01$ and $\phi = \pi/4$. (a) Longitudinal velocity. (b) Transversal velocity profile at the middle plane, $\eta = 0.5$. These plots are valid for $10^{-1} \leq \mathrm{Ra} \leq 10$.

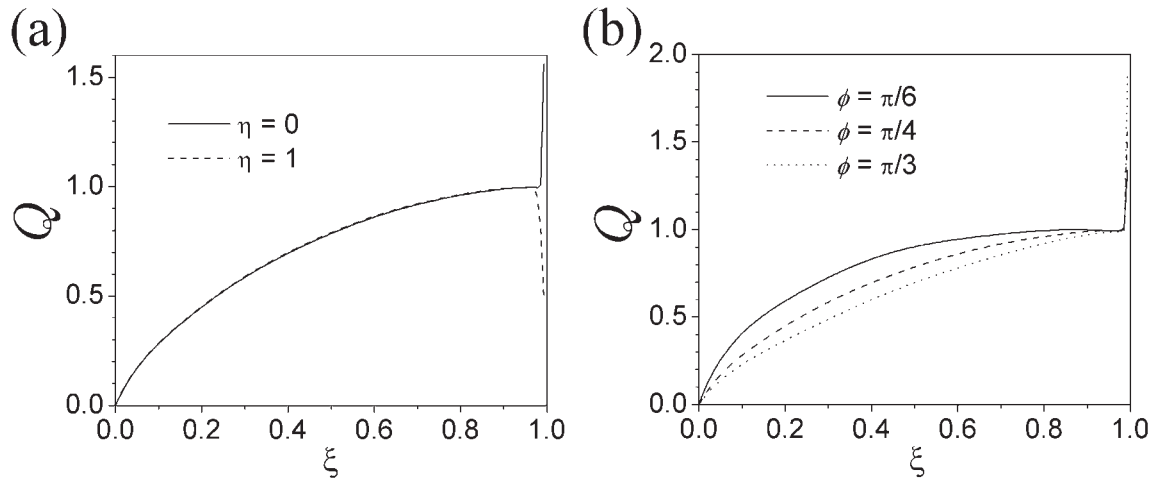

Fig. 12. Dimensionless local heat flux at the longitudinal walls when $\mathrm{Pr} = 0.3645$, $\kappa \ll 1$, $\Gamma = 0.01$. (a) At the lower ($\eta = 0$) and upper ($\eta = 1$) walls when $\phi = \pi/4$. (b) Effect of the angle ϕ on the dimensionless local heat flux at the lower wall, $\eta = 0$. These plots are valid for $10^{-1} \leq \mathrm{Ra} \leq 10$ for the fluid filled layer, and for $10^{-7} \leq \mathrm{Ra} \leq 10^{-3}$ for the saturated porous layer.

differences between opposite points on the longitudinal contact surfaces decreases (Fig. 6), but the longitudinal component of g also increases, so the net buoyancy augments when ϕ raises.

The heat transfer mechanism through the fluid layer is measured by the dimensionless local heat flux Q defined as:

$$Q = -\frac{\partial\theta}{\partial y} = \frac{qd}{k_f(T_\mathrm{H} - T_\mathrm{C})}, \tag{35}$$

where q is the local heat flux and k_f is the fluid thermal conductivity. Figure 12(a) shows the variation of the dimensionless local heat flux at the upper and lower solid–fluid interfaces. These results correspond to $\mathrm{Pr} = 0.3645$, $\kappa \ll 1$, $\Gamma = 0.01$ when $\phi = \pi/4$. Both curves in Fig. 12(a) differ each other only near the upper corner, that because when $\xi \to 1$, the temperature gradient near the upper wall ($\eta = 1$) is smaller than that corresponding to the lower one ($\eta = 0$), see any plot in Fig. 6. The effect of ϕ on the dimensionless local heat flux at $\eta = 0$ is presented in Fig. 12(b), for the case of $\mathrm{Pr} = 0.3645$, $\kappa \ll 1$, $\Gamma = 0.01$. If the tilting angle ϕ increases the temperature differences between opposite points on the longitudinal contact surfaces decreases (see Fig. 6), hence the local heat flux diminishes when ϕ raises. Since the fluid layer is under the conduction regime, Figs. 12(a) and 12(b) are given for $10^{-1} \leq \mathrm{Ra} \leq 10$.

The global heat transfer through the longitudinal walls is measured by the average Nusselt number, $\mathrm{Nu_{av}}$, which is defined as follows:

$$\mathrm{Nu_{av}} = \frac{h_\mathrm{c} d}{k_f}, \tag{36}$$

where h_c is the average convection coefficient. It is easy to show that for the present analysis such average Nusselt number is related to the dimensionless local heat flux as follows:

$$\mathrm{Nu_{av}} = \int_0^1 \left[-\frac{\partial\theta}{\partial y}\right] \mathrm{d}\xi. \tag{37}$$

Figure 13 shows the effect of the tilting angle ϕ on $\mathrm{Nu_{av}}$. As the local heat flux decreases with ϕ, the average Nusselt does too. Since the layer is under the conduction regime, the dimensionless heat flux does not depend on the Rayleigh number, then, Figs. 12 and 13 are valid for $10^{-1} \leq \mathrm{Ra} \leq 10$, and for the motionless fluid layer too. Foregoing remarks reveals that the weak convection flow does not improve the heat transfer phenomena respect to the pure conduction condition, however, such convection flow in fluid layers has proved to be a condition that improves the transport of minerals or contaminants, phenomenon of enormous consequences on geological time scales.[6)]

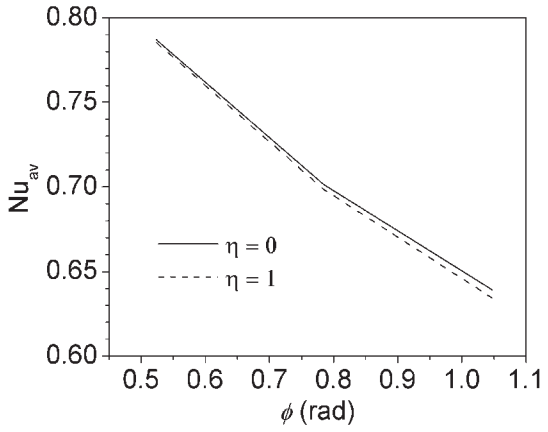

Fig. 13. Effect of the angle ϕ on the average Nusselt number at the lower ($\eta = 0$) and upper ($\eta = 1$) longitudinal walls. These plots are valid for $10^{-1} \leq \mathrm{Ra} \leq 10$ for the fluid filled layer, and for $10^{-7} \leq \mathrm{Ra} \leq 10^{-3}$ for the saturated porous layer.

6.3 The saturated porous layer

Because of the small Rayleigh numbers analyzed in this work, the saturated porous layer was found to be under the conduction regime. So, the previous results involving the temperature distribution within the fluid layer also apply for the saturated porous layer. Indeed, since the Rayleigh numbers are small, the resulting weak convective flows do not affect the isotherms at all. So, the temperature distributions within the porous layer are the same shown in Fig. 6. Such plots are valid for the whole range of the Rayleigh number here studied for the porous layer, $10^{-7} \leq$

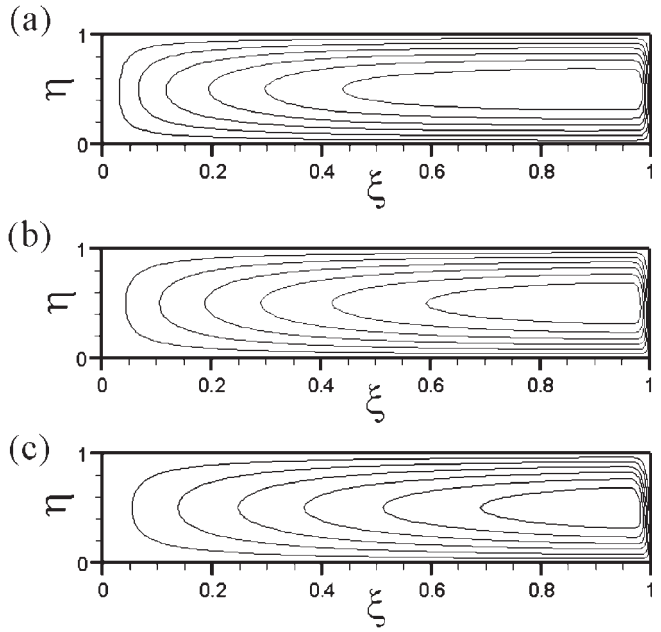

Fig. 14. Effect of the angle ϕ on the convective flow within the saturated porous layer. For all cases $\mathrm{Pr} = 0.3645$, $\kappa \ll 1$, $\Gamma = 0.01$. (a) $\phi = \pi/6$. (b) $\phi = \pi/4$. (c) $\phi = \pi/3$. These plots are valid for $10^{-7} \leq \mathrm{Ra} \leq 10^{-3}$.

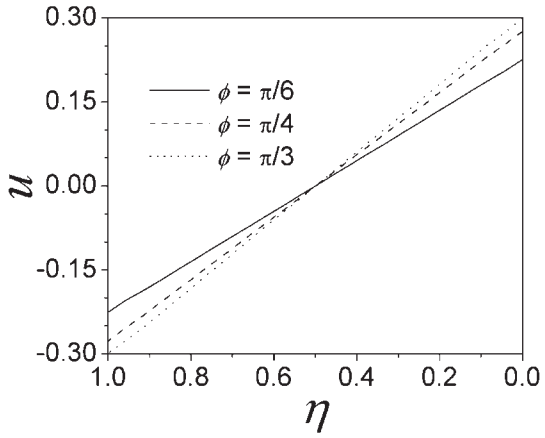

Fig. 16. Effect of the angle ϕ on the longitudinal velocity within the saturated porous layer. For all cases $\mathrm{Pr} = 0.3645$, $\Gamma = 0.01$. All profiles correspond to the velocity u at the middle plane, $\xi = 0.5$. These plots are valid for $10^{-7} \leq \mathrm{Ra} \leq 10^{-3}$.

$\mathrm{Ra} \leq 10^{-3}$, and for the reference case (the motionless saturated porous layer), also. Thus, figures referenced henceforth corresponding to the temperature distribution, heat flux and Nusselt number are valid in this range and for the motionless state, too.

The resulting convection flows are shown in Fig. 14, where numerical results for the stream function in the non-orthogonal coordinate system are plotted for different values of ϕ, when $\mathrm{Pr} = 0.3645$, $\kappa \ll 1$, $\Gamma = 0.01$. The Rayleigh number do not affect the shape of the convective patterns but the angle ϕ does, so, Figure 14 is valid for $10^{-7} \leq \mathrm{Ra} \leq 10^{-3}$. Therefore, figures referenced henceforth corresponding to the filtration velocity are valid in this range.

The circulation patterns are counterclockwise, the flows arise longitudinally near the lower wall and descend near the upper one. Numerical results for the dimensionless velocity profiles at different locations within the porous layer are shown in Fig. 15. The longitudinal velocity profiles are presented in Fig. 15(a). These profiles are symmetrical respect to the middle plane $\eta = 0.5$, as the fluid is warmed while it travels along the lower wall, the flow is faster at the upper region. The transversal velocity profile at the middle plane, $\eta = 0.5$ is shown in Fig. 15(b). The effect of the Rayleigh number on the *actual* velocity has been considered in the definition of the dimensionless velocity itself. The tilting angle ϕ affects the longitudinal dimensionless velocity as it is shown in Fig. 16, where all profiles correspond to the velocity u at the middle plane, $\xi = 0.5$.

The heat transfer mechanism through the saturated porous layer is measured by the dimensionless local heat flux defined in eq. (35), where for this case k_f is equal to the effective thermal conductivity of the porous medium. Since the temperature distribution within the porous layer is the same to that corresponding to the fluid layer, the plot of the dimensionless local heat flux, Fig. 12(a), is also valid for the

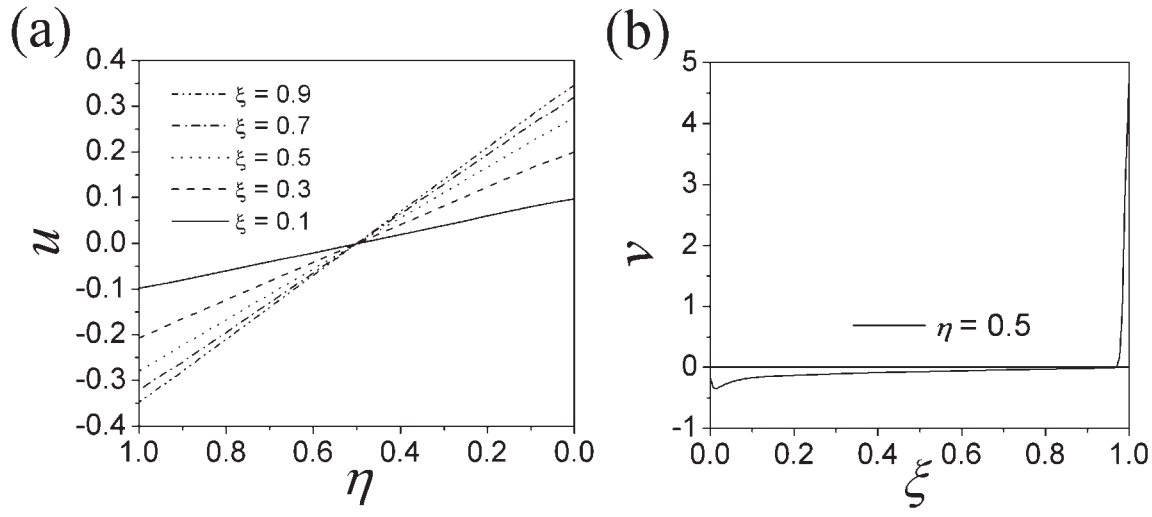

Fig. 15. Velocity profiles at different locations within the saturated porous layer when $\mathrm{Pr} = 0.3645$, $\Gamma = 0.01$ and $\phi = \pi/4$. (a) Longitudinal velocity. (b) Transversal velocity profile at the middle plane, $\eta = 0.5$. These plots are valid for $10^{-7} \leq \mathrm{Ra} \leq 10^{-3}$.

porous layer when $\mathrm{Pr} = 0.3645$, $\kappa \ll 1$, $\Gamma = 0.01$ and $\phi = \pi/4$. Moreover, Fig. 12(b) applies for the porous layer and describes the effect of ϕ on the dimensionless local heat flux at $\eta = 0$, for the case of $\mathrm{Pr} = 0.3645$, $\kappa \ll 1$, $\Gamma = 0.01$. Again, the average Nusselt number, $\mathrm{Nu}_{\mathrm{av}}$ [as defined in eq. (36), where k_f is equal to the effective thermal conductivity of the porous medium], does not depend on the Rayleigh number but it does on the tilting angle ϕ. Then, it is plain that convection flow does not improve the heat transfer phenomena respect to the pure conduction condition, however such weak convection flows in porous media get particular importance when they are involved in the transport of minerals or contaminants on geological time scales.[1,3)]

7. Conclusions

It has been presented an analysis of the steady thermal convection within two, symmetrically interconnected finite layers which are embedded in an impervious rock that is affected by a vertical temperature gradient. It was assumed that the thermal conductivity of the rock is much larger than that of the material which fills the layer, as in typical water or oil reservoirs. The Prandtl number used for the numerical solutions was $\mathrm{Pr} = 0.36$, which corresponds to a typical value for oil at deposit conditions. The temperature distribution in the rock depends on the layer aspect ratio, the layer-material to rock thermal conductivity ratio and the layer inclination. Numerical solutions for the thermal distribution in the rock and the convective flow were computed. Due to the simplicity of experimental realization, measurements were made in a fluid layer using infrared thermography and PIV, and it was found a good agreement with our numerical results. This good matching also brings confidence on the reliability of our numerical results for the porous layer. For both cases, fluid and porous layer, the convective velocity fields were calculated for small Rayleigh numbers, what leads to the conduction regime. In this limit, the temperature distribution within the layer, the convective patterns and the dimensionless velocity do not depend on the Rayleigh number. For the problem here studied, there is no motionless state, however, such a state was used as a reference case to compare with the weak convective condition. It was found that the resulting convection flow does not improve the heat transfer phenomenon respect to the motionless state, then, from a thermal point of view, the tilted fluid layer may be regarded as a *frozen* solid layer with the same thermal conductivity. On the other hand, it was observed a considerable effect of the tilting angle ϕ on the temperature distribution in the rock, and hence the important role this angle plays in the convective motion and heat transfer through the layers. There were not found multicellular structures like those occurring in the secondary flow in a vertical cavity. The experimental measurement showed that there is a quasi-stagnant region at the upper corner and no mass exchange between the two layers was found. The present work shows results that can improve the understanding of transport phenomena not only concerned with heat transfer but also with the oil and underground water pollution problems. Indeed, despite the fact that the convective motion and heat transfer are weak, the present results are useful for the analysis of phenomena that take place on geological scales. Slow convection flows within fluid layers and porous layers have proved to be conditions that improve the transport of minerals or contaminants, phenomena of enormous importance on geological time scales.[1,3,6)] Their consequences like cementation and dissolution of minerals in the rock, or contaminant infiltration into water reservoirs are closely related not only to the convective motion but also with the temperature distribution in the layer and rock, both caused by the ubiquitous geothermal gradient.[10)] Some results related to the present problem, particularly the cases of a single finite length fracture and multifracture configurations have been presented elsewhere,[8)] and further work related to the transport of a passive species within this kind of systems is currently in progress.

Acknowledgments

F.S. acknowledges to "*Programa de Estancias de Entrenamiento en Yacimientos, Instituto Mexicano del Petróleo*". A.M. acknowledges support from Spain Ministerio de Educación, Cultura y Deporte through a sabbatical fellowship Project SAB2002-0137, and from Instituto Mexicano del Petróleo through FIES R1000.

Appendix: Functions Referenced in the Body Text

Functions A to N in eq. (21) are as follows:

$$A = -\frac{\mathrm{Pr}}{\mathrm{Ra}(1+\varepsilon\eta)^4}\left(\frac{\varepsilon^4\xi^4}{\Gamma^2} + \Gamma^2 + 2\varepsilon^2\xi^2\right) \tag{A·1}$$

$$B = \frac{4\mathrm{Pr}\varepsilon\xi}{\mathrm{Ra}(1+\varepsilon\eta)^3}\left(\frac{\varepsilon^2\xi^2}{\Gamma^2} + 1\right) \tag{A·2}$$

$$C = -\frac{12\mathrm{Pr}\varepsilon^2\xi}{\mathrm{Ra}(1+\varepsilon\eta)^4}\left(\frac{\varepsilon^2\xi^2}{\Gamma^2} + 1\right) + \frac{1}{(1+\varepsilon\eta)^3} \times \left[\left(\frac{\partial\psi^0}{\partial y}\right)\left(\Gamma^2 + \varepsilon^2\xi^2\right) + \left(\frac{\partial\psi^0}{\partial x}\right)\left(\varepsilon\Gamma^2\xi + \varepsilon^3\xi^3\right)\right] \tag{A·3}$$

$$D = -\frac{12\mathrm{Pr}\varepsilon^2}{\mathrm{Ra}(1+\varepsilon\eta)^4}\left(\frac{3\varepsilon^2\xi^2}{\Gamma^2} + 1\right) + \frac{1}{(1+\varepsilon\eta)^3}\left[\left(\frac{\partial\psi^0}{\partial y}\right)4\varepsilon^2\xi + \left(\frac{\partial\psi^0}{\partial x}\right)\left(6\varepsilon^3\xi^2 + 2\varepsilon\Gamma^2\right)\right] \tag{A·4}$$

$$E = \frac{8\mathrm{Pr}\varepsilon}{\mathrm{Ra}(1+\varepsilon\eta)^3}\left(\frac{3\varepsilon^2\xi^2}{\Gamma^2} + 1\right) - \frac{1}{(1+\varepsilon\eta)^2}\left[\left(\frac{\partial\psi^0}{\partial y}\right)2\varepsilon\xi + \left(\frac{\partial\psi^0}{\partial x}\right)\left(\Gamma^2 + 3\varepsilon^2\xi^2\right)\right] \tag{A·5}$$

$$F = -\frac{2\mathrm{Pr}}{\mathrm{Ra}(1+\varepsilon\eta)^2}\left(\frac{3\varepsilon^2\xi^2}{\Gamma^2} + 1\right) \tag{A·6}$$

$$G = -\frac{24\varepsilon^4\xi\mathrm{Pr}}{\mathrm{Ra}\Gamma^2(1+\varepsilon\eta)^4} + \frac{2\varepsilon^2}{(1+\varepsilon\eta)^3}\left[\left(\frac{\partial\psi^0}{\partial y}\right) + 3\varepsilon\xi\left(\frac{\partial\psi^0}{\partial x}\right)\right] \tag{A·7}$$

$$H = \frac{24\varepsilon^3\xi\mathrm{Pr}}{\mathrm{Ra}\Gamma^2(1+\varepsilon\eta)^3} - \frac{2\varepsilon}{(1+\varepsilon\eta)^2}\left[\left(\frac{\partial\psi^0}{\partial y}\right) + 3\varepsilon\xi\left(\frac{\partial\psi^0}{\partial x}\right)\right] \tag{A·8}$$

$$I = -\frac{12\varepsilon^2\xi \mathrm{Pr}}{\mathrm{Ra}\Gamma^2(1+\varepsilon\eta)^2} + \frac{1}{1+\varepsilon\eta}\left[\left(\frac{\partial\psi^0}{\partial y}\right) + 3\varepsilon\xi\left(\frac{\partial\psi^0}{\partial x}\right)\right] \tag{A·9}$$

$$J = \frac{4\varepsilon\xi \mathrm{Pr}}{\mathrm{Ra}\Gamma^2(1+\varepsilon\eta)} \tag{A·10}$$

$$K = -\left(\frac{\partial\psi^0}{\partial x}\right) \tag{A·11}$$

$$L = -\frac{\mathrm{Pr}}{\mathrm{Ra}\Gamma^2} \tag{A·12}$$

$$M = -\frac{\mathrm{Pr}}{\mathrm{Ra}\Gamma^2(1+\varepsilon\eta)}\left(\frac{\varepsilon\xi\sin(\phi)}{\Gamma} + \cos(\phi)\right) \tag{A·13}$$

$$N = \frac{\mathrm{Pr}\sin(\phi)}{\mathrm{Ra}\Gamma^3} \tag{A·14}$$

For the case of the fluid layer, functions R to V in eq. (22) are:

$$R = \left(\frac{\partial\psi^0}{\partial y}\right)\frac{1}{1+\varepsilon\eta} + \left(\frac{\partial\psi^0}{\partial x}\right)\frac{\varepsilon\xi}{1+\varepsilon\eta} - \frac{2\varepsilon^2\xi}{\mathrm{Ra}\Gamma^2(1+\varepsilon\eta)^2} \tag{A·15}$$

$$S = -\frac{1}{\mathrm{Ra}\left(1+\varepsilon\eta\right)^2} - \frac{1}{\mathrm{Ra}\Gamma^2}\left(\frac{\varepsilon\xi}{1+\varepsilon\eta}\right)^2 \tag{A·16}$$

$$T = \frac{2\varepsilon\xi}{\mathrm{Ra}\Gamma^2(1+\varepsilon\eta)} \tag{A·17}$$

$$U = -\frac{1}{\mathrm{Ra}\Gamma^2} \tag{A·18}$$

$$V = -\left(\frac{\partial\psi^0}{\partial x}\right) \tag{A·19}$$

where

$$\frac{\partial\psi^0}{\partial x} = \frac{1}{1+\varepsilon\eta}\frac{\partial\psi^0}{\partial\xi} \tag{A·20}$$

and

$$\frac{\partial\psi^0}{\partial y} = \frac{\partial\psi^0}{\partial\eta} - \frac{\varepsilon\xi}{1+\varepsilon\eta}\frac{\partial\psi^0}{\partial\xi} \tag{A·21}$$

Functions A to F in eq. (28) are:

$$A = \frac{2\varepsilon^2\xi}{\left(1+\varepsilon\eta\right)^2} \tag{A·22}$$

$$B = \left(\frac{\varepsilon\xi}{1+\varepsilon\eta}\right)^2 + \left(\frac{\Gamma}{1+\varepsilon\eta}\right)^2 \tag{A·23}$$

$$C = -\frac{2\varepsilon\xi}{1+\varepsilon\eta} \tag{A·24}$$

$$D = 1 \tag{A·25}$$

$$E = -\left(\frac{\sin(\phi)\varepsilon\xi}{1+\varepsilon\eta} + \frac{\Gamma\cos(\phi)}{1+\varepsilon\eta}\right) \tag{A·26}$$

$$F = \sin(\phi) \tag{A·27}$$

For the case of saturated porous layer, functions R to V in eq. (22) are:

$$R = \left(\frac{\partial\psi^0}{\partial y}\right)\frac{1}{1+\varepsilon\eta} + \left(\frac{\partial\psi^0}{\partial x}\right)\frac{\varepsilon\xi}{1+\varepsilon\eta} - \frac{2\varepsilon^2\xi}{\Gamma\mathrm{Ra}\left(1+\varepsilon\eta\right)^2} \tag{A·28}$$

$$S = -\frac{\Gamma}{\mathrm{Ra}\left(1+\varepsilon\eta\right)^2} - \frac{1}{\Gamma\mathrm{Ra}}\left(\frac{\varepsilon\xi}{1+\varepsilon\eta}\right)^2 \tag{A·29}$$

$$T = \frac{2\varepsilon\xi}{\Gamma\mathrm{Ra}\left(1+\varepsilon\eta\right)} \tag{A·30}$$

$$U = -\frac{1}{\Gamma\mathrm{Ra}} \tag{A·31}$$

$$V = -\left(\frac{\partial\psi^0}{\partial x}\right) \tag{A·32}$$

1) O. M. Phillips: *Flow and Reactions in Permeable Rocks* (Cambridge University Press, Cambridge, 1991).
2) J. R. Wood and T. A. Hewett: Geochem. Cosmochem. Acta **46** (1982) 1707.
3) T. A. Hewett: in *Reservoir characterization*, ed. L. W. Lake and H. B. Carroll, Jr. (Academic Press, Orlando, FL, 1986) p. 83.
4) S. H. Davies, S. Rosenblat, J. R. Wood and T. A. Hewett: Am. J. Sci. **285** (1985) 207.
5) S. J. Linz and A. W. Woods: Phys. Rev. A **46** (1992) 4869.
6) A. W. Woods and S. J. Linz: J. Fluid Mech. **241** (1992) 59.
7) E. Luna, J. A. Cordova, A. Medina and F. J. Higuera: Phys. Lett. A **300** (2002) 449.
8) A. Medina, E. Luna, C. Pérez-Rosales and F. J. Higuera: J. Phys.: Condens. Matter **14** (2002) 2467.
9) J. Bear: *Dynamics of Fluids in Porous Media* (Dover Publications, New York, 1972).
10) E. Luna, A. Medina, C. Treviño and C. Pérez-Rosales: J. Porous Media **7** (2004) 303.